ON MEASURING INNER HALO PROFILES WITH WEAK LENSING SHEAR AND MAGNIFICATION

Matthew R. George
Department of Astronomy, University of California, Berkeley and
Lawrence Berkeley National Laboratory, 1 Cyclotron Road, Berkeley, CA 94720, USA
Draft version September 9, 2013

ABSTRACT

We report how weak lensing can constrain mass profiles on small scales within dark matter halos. We forecast constraints for shear and magnification measurements using a Markov chain Monte Carlo approach with parametric models for the mass profile, exploring the dependence on the minimum radius measured, survey area and source number density, and the mass of the lens galaxies. If observational systematics can be controlled, future surveys will be capable of differentiating between models of baryonic contraction, cooling, and feedback using weak lensing alone. Such measurements will also constrain the stellar mass-to-light ratio without any model assumptions about the initial mass function or star formation history. These results provide motivation for minimizing observational systematics on small scales, since a careful accounting of baryonic contributions to the mass profile will inform our understanding of galaxy evolution and will also be important for achieving the cosmological goals of lensing surveys.

1. INTRODUCTION

We want to measure the shape of the dark matter profile on small scales. This will tell us how baryons have affected the dark matter distribution, the assembly history of the baryons and dark matter as well as feedback processes, and whether dark matter interacts to form "cored" profiles as opposed to the "cuspy" profiles seen in cold dark matter simulations. Measurements of the mass distribution on scales comparable to the effective radius of a galaxy can also constrain the mass-to-light ratio of the stellar population which is uncertain by a factor of ~ 2 depending on the initial mass function which is generally assumed.

Earlier baryonic effects on lensing, e.g. Kochanek and White

SIDM review?

baryonic effects on cosmic shear, White, Rudd et al, Zentner et al.

Add para on small-scale systematics, motivation is to see what we can learn by pushing WL down to smaller scales.

Various observational probes have been used to constrain the mass profile of galaxies and dark matter halos, typically with dynamical measurements within a few kpc of the galaxy center, stong lensing arcs a bit farther out, and weak lensing on larger scales to measure the total mass of the halo (e.g., Sand et al. 2004; Koopmans et al. 2006; Gavazzi et al. 2007; Jiang & Kochanek 2007; Auger et al. 2010; Schulz et al. 2010; Newman et al. 2013). While central velocity dispersions or rotation curves can be measured for large samples of galaxies, detailed kinematic measures on scales $\gtrsim 10\,\mathrm{kpc}$ are difficult and strong lenses exist in only a sparse sample of the galaxy population. Weak lensing, on the other hand, can probe the average profile for large samples of galaxies, allowing studies of population differences and redshift evolution, independent of their dynamical state. For instance, the assembly histories of disk and elliptical galaxies may dif-fer and hydrodynamical simulations predict significant differences in the inner profiles of their dark matter halos. Additionally, weak lensing shear and magnification have different scale-dependence on the surface mass density profile providing added leverage in constraining its shape. The aim of this letter is to investigate how well weak lensing shear and magnification can constrain the inner mass profile of dark matter halos and galaxies.

Several authors have studied the complementarity of shear and magnification, primarily for measuring halo masses (Bartelmann et al. 1996; Bridle et al. 1998; Schneider et al. 2000; van Waerbeke et al. 2010; Rozo & Schmidt 2010; Umetsu et al. 2011) or probing the matter distribution on cosmological scales (van Waerbeke 2010; Casaponsa et al. 2013; Duncan et al. 2013; Krause et al. 2013). Combining shear and magnification increases the statistical precision of a lensing experiment and also enables tests of systematic effects which differ between probes.

While weak lensing experiments traditionally measure galaxy ellipticities to infer the shear signal, magnification can be measured using sizes (Bartelmann & Narayan 1995), fluxes (Broadhurst et al. 1995), or by combining the two (Huff & Graves 2011; Schmidt et al. 2012). Magnification has recently been measured with signal-to-noise approaching that from shear for ensembles of galaxies (Scranton et al. 2005; Hildebrandt et al. 2009; Ménard et al. 2010; Huff & Graves 2011; Ford et al. 2012; Schmidt et al. 2012).

THIS PAPER

We define halos within a virial overdensity of 200 times the critical density of the Universe and use physical distances with $h = 0.7, \Omega_m = 0.3, \Omega_\Lambda = 0.7$. Logarithmic quantities denoted with log and ln implicitly use base ten and e respectively. Radii are denoted by r for three-dimensional profiles and R for projected, two-dimensional profiles.

mgeorge@astro.berkeley.edu

2. LENS MODELING

The distortion of galaxy images due to weak lensing can be described by a matrix written in terms of the convergence κ and shear components γ_1, γ_2 (e.g. Bartelmann & Schneider 2001):

$$A = \begin{pmatrix} 1 - \kappa - \gamma_1 & -\gamma_2 \\ -\gamma_2 & 1 - \kappa + \gamma_1 \end{pmatrix}. \qquad (1)$$

From galaxy images, one can measure the magnification $\mu = (\det A)^{-1} = [(1-\kappa)^2 - |\gamma|^2]^{-1} \approx 1 + 2\kappa$ and reduced shear $g = \gamma/(1 - \kappa) \approx \gamma$, where we have defined the complex shear $\gamma = \gamma_1 + i\gamma_2$ and approximations are given to first order in the weak limit $|\gamma|, \kappa \ll 1$.

The convergence and tangential component of shear can be related to the projected surface mass density Σ of the lens via

$$\kappa = \frac{\Sigma}{\Sigma_c}; \ \ \gamma_t = \frac{\Delta\Sigma}{\Sigma_c} \qquad (2)$$

where the critical surface density Σ_c is a function of the angular diameter distances between the observer (o), lens (l), and source (s),

$$\Sigma_c = \frac{c^2}{4\pi G} \frac{D_{os}}{D_{ol} D_{ls}}. \qquad (3)$$

A typical galaxy lensing experiment averages measurements of g_t or μ in bins of radius R around the lens position to constrain its radial surface density profile (or stacks many such measurements for an ensemble of lenses). Magnification directly probes the surface density at a given position $\Sigma(R)$, whereas shear is sensitive to the excess surface density interior to the projected radius $\Delta\Sigma(R) = \overline{\Sigma}(< R) - \overline{\Sigma}(R)$. This difference in scale-dependence is what we hope to exploit by combining shear and magnification measurements to constrain inner halo profiles.

We consider parametric models for the three-dimensional density profile $\rho(r)$ of the lens galaxy and dark matter halo, which are then projected into two dimensions for comparison with the lensing observables. The stellar component is modeled as a Hernquist (1990) profile of the form

$$\rho_\star(r) = \frac{M_\star}{2\pi} \frac{a}{r(r + r_\star)^3} \qquad (4)$$

parametrized by the total stellar mass $M_\star$ and scale radius $r_\star$, which is a good description of elliptical galaxies. If a constant stellar mass-to-light ratio is assumed, the projected scale radius $R_{\rm deV}$ measured from fitting a de Vaucouleurs model to the surface brightness profile of the galaxy can be converted to the three-dimensional Hernquist radius using $R_{\rm deV} = 1.8153\, r_\star$. Stellar masses are typically estimated by modeling the spectral energy distribution of a galaxy, but assumptions in this process lead to significant systematic uncertainties dominated by our ignorance of the stellar initial mass function (IMF). We will treat $M_\star$ as a free parameter to determine how well lensing can constrain these uncertainties.

Our baseline model for the dark matter halo is the Navarro-Frenk-White (NFW, Navarro et al. 1996) profile with parameters for the halo mass M_h and concentration c. Wright & Brainerd (2000) give projections of this profile to compute $\Sigma_{\rm NFW}$ and $\Delta\Sigma_{\rm NFW}$.

The NFW model was introduced to describe the form of halos in dark matter simulations, but baryonic processes including cooling and feedback can modify the shape of the dark matter profile (e.g., Blumenthal et al. 1986; Gao et al. 2004; Gnedin et al. 2004; Johansson et al. 2009; Abadi et al. 2010; Gnedin et al. 2011). Because we lack a good physical description of these processes, we consider a variable amount of halo contraction or expansion using the model of Dutton et al. (2007). This model assumes the quantity $rM(r)^\nu$ is conserved during the formation of a galaxy, with both baryons and dark matter initially distributed following an NFW profile, and the baryons eventually collapsing into a final distribution which we take to be $\rho_\star(r)$ from Equation 4. The parameter ν controls the amount of contraction, with $\nu = 1$ recovering the adiabatic contraction (AC) model of Blumenthal et al. (1986), $\nu = 0$ giving an uncontracted NFW profile, and $\nu < 0$ for expansion of the dark matter on small scales. Hydrodynamical simulations predict a range of values $-0.2 \lesssim \nu \lesssim 0.8$ (CHECK?) depending on the details of the cooling and feedback models as well as the assembly history of the galaxy.

Models of halo contraction are typically implemented assuming that the mass within the virial radius is conserved, i.e., that there is no contraction at or beyond the virial radius. While contraction models produce an excess mass density at $r \lesssim r_\star$, this boundary condition leads to a mass *deficit* on intermediate scales between $\sim r_\star$ and the virial radius, and vice versa for expansion models. We demonstrate this effect in Figure 1 showing ρ, Σ, and $\Delta\Sigma$ halo profiles with model parameters given in Table 1. The fiducial NFW profile is compared to models with the same initial halo parameters that have undergone expansion ($\nu = -0.2$) or adiabatic contraction. To compute the projected profiles we extrapolate $\rho(r)$ beyond the virial radius using the initial NFW profile. The AC model deviates by $\sim 25\%$ from the corresponding NFW model at scales of tens of kiloparsecs. We also see that the shear and magnification observables have different scale-dependence demonstrating their complementarity.

Figure 1 includes a stellar profile for comparison to the halo models. The stars fall off much more rapidly than the dark matter and the transition between the excess and deficit regions for the AC model relative to NFW occurs at roughly the scale where stars and dark matter contribute equally to the total profile. In practice, lensing can only measure the sum of the stellar and dark matter components but we separate these components in the figure to isolate the contraction/expansion effects.

The contraction model depends on the ratios $M_\star/M_h$ and $r_\star/r_h$, with greater contraction for galaxies that are more massive and compact relative to their halos. For a galaxy with $M_\star = 10^{11}\, M_\odot, R_{\rm deV} = 10\,{\rm kpc}\,(r_\star = 5.5\,{\rm kpc})$ in a cluster-scale halo with $M_h = 10^{15}\, M_\odot, c = 5$, the AC and expansion models deviate by less than 3% from the NFW profile at $R > 10\,{\rm kpc}$. The value of $M_\star/M_h$ peaks near $M_\star \approx 10^{10.5}, M_h \approx 10^{12}$ (e.g. Conroy & Wechsler 2009; Behroozi et al. 2010; Leauthaud et al. 2012) which motivates targeting compact galaxies in this mass range to measure baryonic contraction effects, rather than massive clusters or low-mass dwarfs. Additionally, weak lensing measurements are often lim-
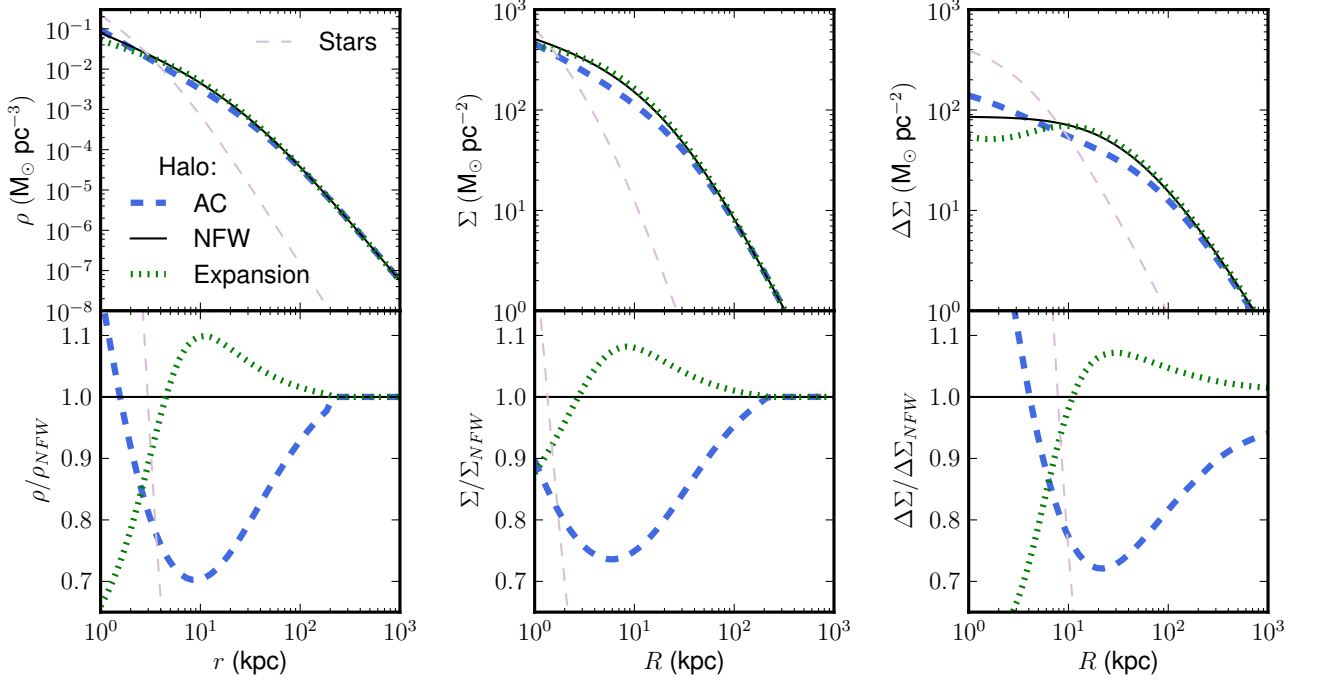
FIG. 1.— Density ($\rho(r)$; left), magnification ($\Sigma(R)$; center), and shear ($\Delta\Sigma(R)$; right) profiles for different halo models showing the effects of baryonic contraction or expansion relative to NFW. A Hernquist profile for the stellar component is included for comparison. Stellar and NFW model parameters are from Table 1. The AC model uses $\nu = 1$ while the Expansion model has $\nu = -0.2$. The boundary condition specifying no contraction at the virial radius leads to a deficit (excess) in the AC (Expansion) profiles relative to NFW at $r_\star \lesssim r \lesssim r_{\rm vir}$.

ited on small angular scales due to systematic effects, so a low-redshift lens sample allows one to probe smaller physical scales where contraction effects are greatest.

3. FORECASTS

To understand how well model halo profiles can be constrained, we need to estimate the signal-to-noise (S/N) of the lensing measurement. We choose two fiducial galaxy models and two sets of survey parameters given in Tables 1 and 2. The fiducial models are constructed as in Section 2, with the total signal composed of the sum of an NFW halo and a Hernquist profile for the stellar component. For each of the the lens samples which have mean stellar masses of $\log(M_\star/M_\odot) = 10.5$ ("Galaxies") and 11.5 ("Clusters"), the halo mass is taken from the mean $M_h(M_\star)$ relation derived from abundance matching (Behroozi et al. 2010) and the concentration is set to the mean $c(M_h)$ relation from recent dark matter simulations (Klypin et al. 2011). The number densities for the lens samples are estimated from a fit to an empirical stellar mass function (Li & White 2009) assuming galaxies are selected in bins of width $\Delta \log(M_\star) = 0.5$ dex and $\Delta z_l = 0.1$. Survey parameters reflect the existing shape catalog in SDSS (Reyes et al. 2012) and anticipated shear data from LSST (Chang et al. 2013).

The measurement uncertainty for shear is assumed to be dominated by intrinsic shape noise and is estimated as

$$\sigma_{\Delta\Sigma} = \frac{\sigma_\gamma \Sigma_c}{\sqrt{n_l A_S n_s \pi (R_2^2 - R_1^2)}} \quad (5)$$

where the denominator is the square root of the number of source-lens pairs in the survey and R_1 and R_2

are the edges of the radial bins. For the shape noise, we take $\sigma_\gamma = 0.25$ as the intrinsic scatter in a single component of γ due to the variety of galaxy ellipticities, noting that this value falls between measured values in SDSS (Hirata et al. 2004) and COSMOS (Leauthaud et al. 2007). The variety of approaches to magnification measurements mentioned in the introduction have differences in their source selection and in the intrinsic scatter for the observable. While these properties differ from shear experiments in general, the measurement uncertainty typically has the same scaling with Σ_c, n_l, A_S, and R. We thus parametrize the measurement uncertainty for magnification with

$$\Gamma = \frac{\sigma_{\Delta\Sigma}}{\sigma_\Sigma} = \frac{\sigma_\gamma}{\sigma_\kappa} \sqrt{\frac{n_{s,\rm mag}}{n_{s,\rm shear}}}, \quad (6)$$

and use values of $\Gamma = 0.5, 1$ to represent current and optimistic magnification measurements. The fiducial models are shown in Figure 2 with measurement errors for each survey plotted in the range $20 - 2000$ kpc with bins of width $\Delta \log(R) = 0.15$.

We have made a number of idealized assumptions since our goal is to illustrate the potential of such measurements and to motivate development of methods to deal with small-scale systematics. For simplicity, we take a single value for the stellar and halo masses as well as the lens and source redshifts, rather than accounting for the full distribution of each parameter. We assume that Σ and $\Delta\Sigma$ can be estimated from magnification and shear observables in an unbiased manner down to our minimum radius ($R_{\rm min} = 20$ or 40 kpc corresponding to angular scales of $\sim 10'', 20''$ at $z_l = 0.1$). For discussion of mod-

TABLE 1
MODEL PARAMETERS

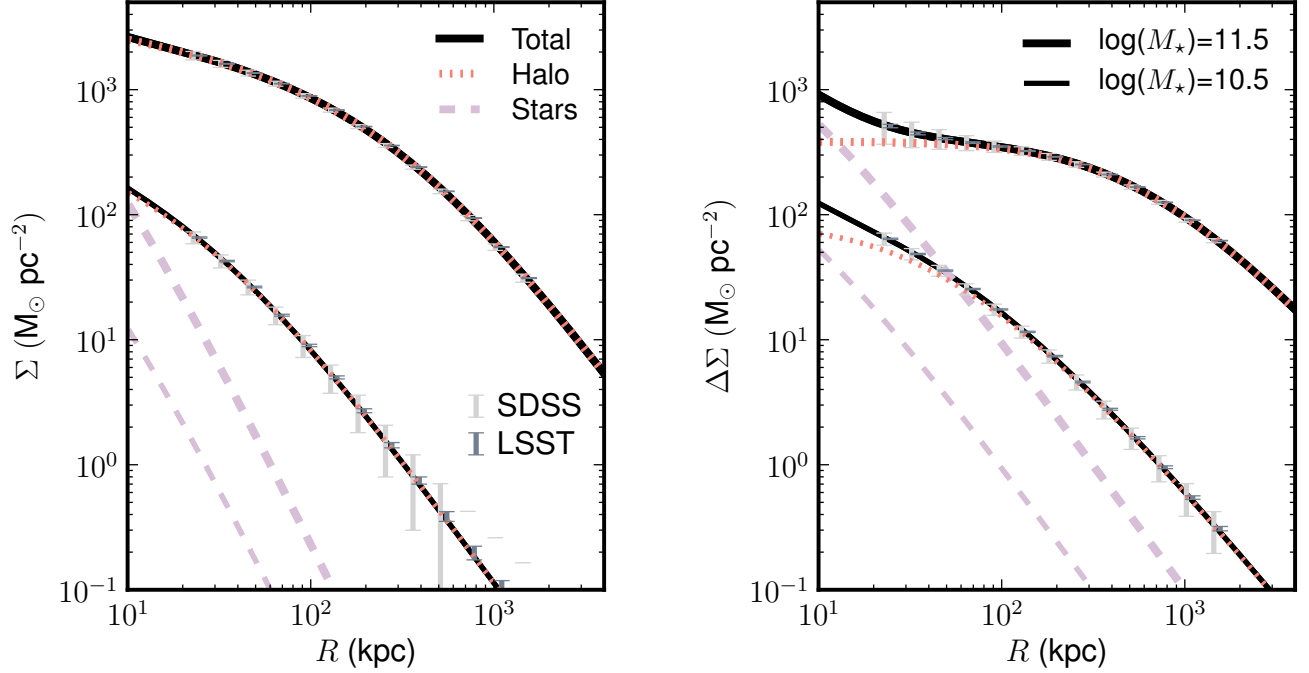| Name	Description	Galaxies	Clusters	Prior
$\log(M_\star)$	Stellar mass ($M_\odot$)	10.5	11.5	Flat[fid.$\pm$0.5]
$\log(r_\star)$	Hernquist radius (kpc)	0.5	0.5	Fixed
$\log(M_h)$	Halo mass ($M_\odot$, $\Delta = 200\rho_c$)	11.968	14.745	Flat[fid.$\pm$0.5]
c	Halo concentration	7.44	4.60	Flat[2,10]; Fixed
ν	Contraction level	0	0	Flat[-0.2, 1.0]
n_l	Lens density (deg^{-2})	39.5	0.0947	-

FIG. 2.— Magnification ($\Sigma(R)$; left) and shear ($\Delta\Sigma(R)$; right) profiles for fiducial galaxy and cluster models with parameters given in Table 1 and error bars predicted from the survey parameters in Table 2. Errors for both surveys on the cluster sample and for LSST on the galaxy sample are similar to the line widths.

TABLE 2
SURVEY PARAMETERS

Name	Description	SDSS	LSST
A_S	Survey area (deg^2)	9243	18000
n_s	Source density (arcmin^{-2})	1.2	37
z_l	Lens redshift	0.1	0.1
z_s	Source redshift	0.39	0.82

eling lensing observables into the nonlinear regime, see Ménard et al. (2003); Takada & Hamana (2003); Mandelbaum et al. (2006). We will also assume these quantities are constrained independently; Rozo & Schmidt (2010) provide a treatment of their covariance. Galaxies are assumed to lie at the centers of their halos; see e.g., Johnston et al. (2007); George et al. (2012) for approaches to treat miscentering.

Constraints on model profiles are derived in a Bayesian sense by sampling the parameter space to maximize the posterior probability of the data given the model and priors. The posterior for a set of model parameters $\boldsymbol{\lambda}$ given the general data set $\boldsymbol{d} = \{\Sigma(R), \Delta\Sigma(R)\}$ is defined

as

$$\ln P(\boldsymbol{\lambda}|\boldsymbol{d}) \propto -\frac{1}{2}\chi^2_{\mathcal{L}}(\boldsymbol{d}|\boldsymbol{\lambda}) + \ln \mathcal{P}(\boldsymbol{\lambda}). \quad (7)$$

The right-hand side consists of the prior $\mathcal{P}$ and the likelihood

$$\chi^2_{\mathcal{L}}(\boldsymbol{d}|\boldsymbol{\lambda}) = \sum_i \left(\frac{\Sigma(R_i|\boldsymbol{\lambda}) - \Sigma(R_i|\hat{\boldsymbol{\lambda}})}{\sigma_\Sigma(R_i)} \right)^2 \\ + \left(\frac{\Delta\Sigma(R_i|\boldsymbol{\lambda}) - \Delta\Sigma(R_i|\hat{\boldsymbol{\lambda}})}{\sigma_{\Delta\Sigma}(R_i)} \right)^2 \quad (8)$$

where $\hat{\boldsymbol{\lambda}}$ is the set of input model parameters. We consider shear and magnification constraints separately in addition to the combined data set, and remove data from the likelihood calculation accordingly.

Sampling is performed using the affine invariant Markov chain Monte Carlo (MCMC) algorithm of Goodman & Weare (2010) implemented in the emcee code of Foreman-Mackey et al. (2013). We opt for a Monte Carlo approach rather than Fisher information since it is more

robust to non-Gaussianity and nontrivial degeneracies in the likelihood surface, which are observed in some cases. Priors are listed in Table 1. We use flat priors with finite ranges to restrict the parameter space searched, setting $\mathcal{P}$ to a constant within the specified range and $-\infty$ outside. The ranges for $M_\star$ and M_h are centered on the fiducial values, while ν and c are allowed to vary over a plausible range borrowed from simulations. Since these parameters are somewhat degenerate, we also test fixing the concentration to the fiducial value, assuming that dark matter simulations can provide reliable halo concentrations before any baryonic contraction or expansion effects modify the halo.

Results in Figures 3 and 4 and Table 3.

4. DISCUSSION

[PRELIMINARY DISCUSSION] It looks like $M_\star$ and M_h can be constrained well, but only one of c or ν can be constrained with lower quality data since they show a significant degeneracy. I would argue that c can be reasonably estimated from dark matter simulations, so we can fix it to constrain ν, which is much less well-understood from hydrodynamical simulations. If the *wrong* c is assumed, shear and magnification observables give inconsistent constraints on $M_\star$ and M_h, which can provide a useful test of the assumed c. It is also interesting that $M_\star$ can be constrained from lensing alone, which will help determine the IMF. Even though we assume a Hernquist profile with a fixed stellar mass to light ratio, the stellar component has a much steeper profile than even an adiabatically contracted halo profile (see Figure 2), so moderate uncertainties in the slope of the stellar component can be tolerated.

REFERENCES

Abadi, M. G., Navarro, J. F., Fardal, M., Babul, A., & Steinmetz, M. 2010, MNRAS, 407, 435
Auger, M. W., Treu, T., Bolton, A. S., Gavazzi, R., Koopmans, L. V. E., Marshall, P. J., Moustakas, L. A., & Burles, S. 2010, ApJ, 724, 511
Bartelmann, M., & Narayan, R. 1995, ApJ, 451, 60
Bartelmann, M., Narayan, R., Seitz, S., & Schneider, P. 1996, ApJ, 464, L115
Bartelmann, M., & Schneider, P. 2001, Phys. Rep., 340, 291
Behroozi, P. S., Conroy, C., & Wechsler, R. H. 2010, ApJ, 717, 379
Blumenthal, G. R., Faber, S. M., Flores, R., & Primack, J. R. 1986, ApJ, 301, 27
Bridle, S. L., Hobson, M. P., Lasenby, A. N., & Saunders, R. 1998, MNRAS, 299, 895
Broadhurst, T. J., Taylor, A. N., & Peacock, J. A. 1995, ApJ, 438, 49
Casaponsa, B., Heavens, A. F., Kitching, T. D., Miller, L., Barreiro, R. B., & Martínez-González, E. 2013, MNRAS, 430, 2844
Chang, C., et al. 2013, MNRAS, 434, 2121
Conroy, C., & Wechsler, R. H. 2009, ApJ, 696, 620
Duncan, C., Joachimi, B., Heavens, A., Heymans, C., & Hildebrandt, H. 2013, ArXiv e-prints
Dutton, A. A., van den Bosch, F. C., Dekel, A., & Courteau, S. 2007, ApJ, 654, 27
Ford, J., et al. 2012, ApJ, 754, 143
Foreman-Mackey, D., Hogg, D. W., Lang, D., & Goodman, J. 2013, PASP, 125, 306
Gao, L., Loeb, A., Peebles, P. J. E., White, S. D. M., & Jenkins, A. 2004, ApJ, 614, 17
Gavazzi, R., Treu, T., Rhodes, J. D., Koopmans, L. V. E., Bolton, A. S., Burles, S., Massey, R. J., & Moustakas, L. A. 2007, ApJ, 667, 176
George, M. R., et al. 2012, ApJ, 757, 2
Gnedin, O. Y., Ceverino, D., Gnedin, N. Y., Klypin, A. A., Kravtsov, A. V., Levine, R., Nagai, D., & Yepes, G. 2011, ArXiv e-prints
Gnedin, O. Y., Kravtsov, A. V., Klypin, A. A., & Nagai, D. 2004, ApJ, 616, 16
Goodman, J., & Weare, J. 2010, Commun. Appl. Math. Comput. Sci., 5, 65
Hernquist, L. 1990, ApJ, 356, 359
Hildebrandt, H., van Waerbeke, L., & Erben, T. 2009, A&A, 507, 683

Hirata, C. M., et al. 2004, MNRAS, 353, 529
Huff, E. M., & Graves, G. J. 2011, ArXiv e-prints
Jiang, G., & Kochanek, C. S. 2007, ApJ, 671, 1568
Johansson, P. H., Naab, T., & Ostriker, J. P. 2009, ApJ, 697, L38
Johnston, D. E., et al. 2007, ArXiv e-prints
Klypin, A. A., Trujillo-Gomez, S., & Primack, J. 2011, ApJ, 740, 102
Koopmans, L. V. E., Treu, T., Bolton, A. S., Burles, S., & Moustakas, L. A. 2006, ApJ, 649, 599
Krause, E., Chang, T.-C., Doré, O., & Umetsu, K. 2013, ApJ, 762, L20
Leauthaud, A., et al. 2007, ApJS, 172, 219
—. 2012, ApJ, 744, 159
Li, C., & White, S. D. M. 2009, MNRAS, 398, 2177
Mandelbaum, R., Seljak, U., Cool, R. J., Blanton, M., Hirata, C. M., & Brinkmann, J. 2006, MNRAS, 372, 758
Ménard, B., Hamana, T., Bartelmann, M., & Yoshida, N. 2003, A&A, 403, 817
Ménard, B., Scranton, R., Fukugita, M., & Richards, G. 2010, MNRAS, 405, 1025
Navarro, J. F., Frenk, C. S., & White, S. D. M. 1996, ApJ, 462, 563
Newman, A. B., Treu, T., Ellis, R. S., Sand, D. J., Nipoti, C., Richard, J., & Jullo, E. 2013, ApJ, 765, 24
Reyes, R., Mandelbaum, R., Gunn, J. E., Nakajima, R., Seljak, U., & Hirata, C. M. 2012, MNRAS, 425, 2610
Rozo, E., & Schmidt, F. 2010, ArXiv e-prints
Sand, D. J., Treu, T., Smith, G. P., & Ellis, R. S. 2004, ApJ, 604, 88
Schmidt, F., Leauthaud, A., Massey, R., Rhodes, J., George, M. R., Koekemoer, A. M., Finoguenov, A., & Tanaka, M. 2012, ApJ, 744, L22
Schneider, P., King, L., & Erben, T. 2000, A&A, 353, 41
Schulz, A. E., Mandelbaum, R., & Padmanabhan, N. 2010, MNRAS, 408, 1463
Scranton, R., et al. 2005, ApJ, 633, 589
Takada, M., & Hamana, T. 2003, MNRAS, 346, 949
Umetsu, K., Broadhurst, T., Zitrin, A., Medezinski, E., & Hsu, L.-Y. 2011, ApJ, 729, 127
van Waerbeke, L. 2010, MNRAS, 401, 2093
van Waerbeke, L., Hildebrandt, H., Ford, J., & Milkeraitis, M. 2010, ApJ, 723, L13
Wright, C. O., & Brainerd, T. G. 2000, ApJ, 534, 34

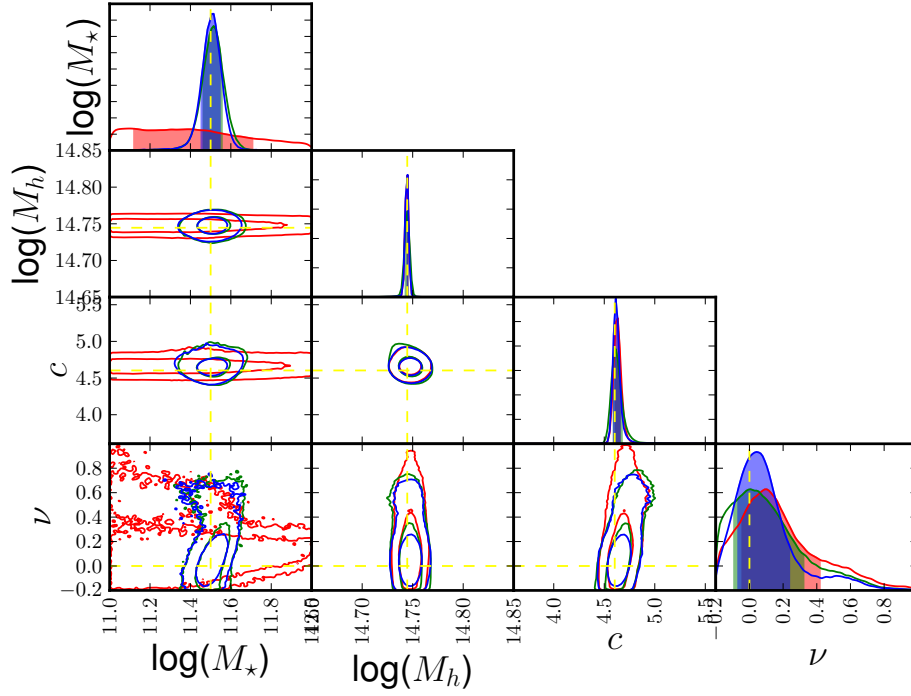FIG. 3.— Posterior distributions for model parameters from MCMC fit with the fiducial Cluster model, LSST survey parameters, $R_{\min} = 20\,\mathrm{kpc}$, and $\Gamma = 1.0$. Contraints are from $\Sigma(R)$ (red), $\Delta\Sigma(R)$ (green), and the combined data (blue). The top column in each panel shows the arbitrarily normalized one-dimensional posterior for each parameter while marginalizing over other parameters, and lower panels show the 68% and 95% contours of the joint posterior distribution for each pair of parameters. In this optimistic scenario, all four parameters are constrained by the data.
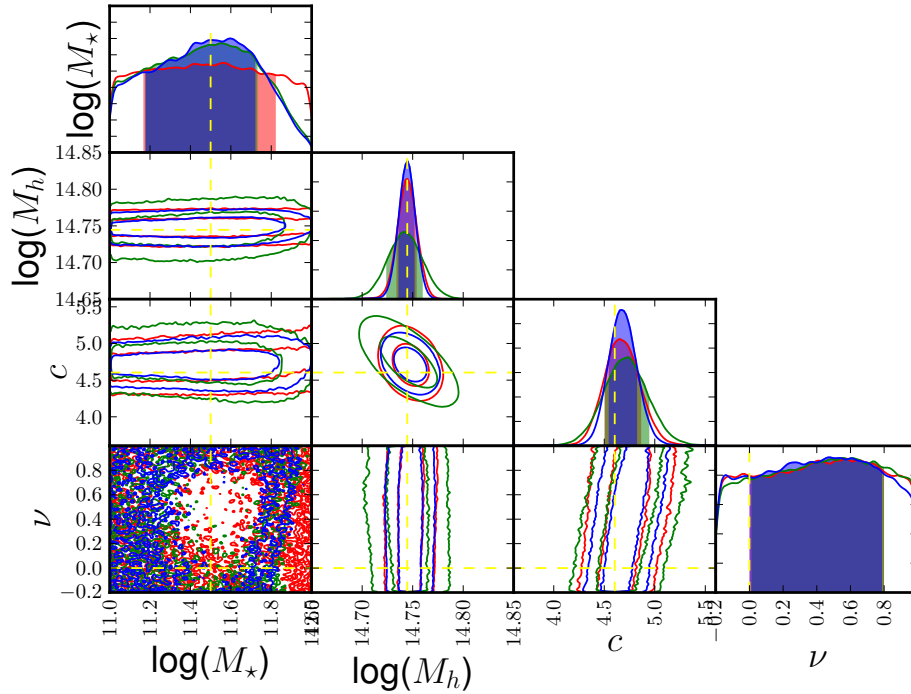

FIG. 4.— Same as Figure 3 but with SDSS survey parameters.

<div align="center">

TABLE 3
PARAMETER CONSTRAINTS

</div>

Description	Galaxies				Clusters			
	$\log(M_\star)$	$\log(M_h)$	c	ν	$\log(M_\star)$	$\log(M_h)$	c	ν
SDSS								
$R_{\min} = 20\,\mathrm{kpc}$								
c fixed, $\Gamma = 0.5$	1	2	3	4	1	2	3	4
c free, $\Gamma = 0.5$	1	2	3	4	1	2	3	4
c fixed, $\Gamma = 1$	1	2	3	4	1	2	3	4
c free, $\Gamma = 1$	1	2	3	4	1	2	3	4
$R_{\min} = 40\,\mathrm{kpc}$								
LSST								
$R_{\min} = 20\,\mathrm{kpc}$								
$R_{\min} = 40\,\mathrm{kpc}$								